

Effect of Glycine-to-nitrate Ratio on Solution Combustion Synthesis of ZnFe₂O₄ as Anode Materials for Lithium Ion Batteries

Jiaming Liu¹, Ding Wang¹, Peng Dong¹, Jinbao Zhao², Qi Meng¹, Yingjie Zhang^{1,*}, Xue Li^{1,*}

¹ National and Local Joint Engineering Laboratory for Lithium-ion Batteries and Materials Preparation Technology, Key Laboratory of Advanced Battery Materials of Yunnan Province, Faculty of Metallurgical and Energy Engineering, Kunming University of Science and Technology, Kunming 650093, China

² State Key Laboratory of Physical Chemistry of Solid Surfaces, Department of Chemistry, College of Chemistry and Chemical Engineering, Xiamen University, 361005, China

Corresponding author: Tel: +86-18808804528

*E-mail: 438616074@qq.com, zyjmust@126.com

Received: 10 January 2017 / Accepted: 28 February 2017 / Published: 12 April 2017

Porous ZnFe₂O₄ nanoparticles have been successfully prepared via solution combustion synthesis, where glycine is used as a fuel and complexant in the combustion reaction. The effects of different glycine-to-nitrate ratio (where ratio equals 0.5, 1.0 and 1.5) on the combustion processes, phase composition, morphology and electrochemical performances of ZnFe₂O₄ are investigated in detail. As the glycine content changing, we can find a regular variation in the exothermic reaction temperature, porous structure and crystallinity. Among three samples, the ratio 1.0 sample reveals the highest crystallinity without any impurity and exhibits a higher rate capability and better reversibility as well. At current density of 1600 mA g⁻¹, its average discharge capacity is 882.1 mAh g⁻¹. When the current density returns to 100 mA g⁻¹, the average discharge capacity recovers to 1232.5 mAh g⁻¹. After 100 cycles at 200 mA g⁻¹, the discharge capacity of ratio 1.0 sample is 1195.3 mAh g⁻¹, which is even higher than the second cycle. The superior electrochemical performances can be attributed to the uniform porous structure in pure phase, which can not only ease the volume expansion during the charge-discharge processes but also provide more interstices for lithium ions insertion. Furthermore, the high crystallinity is able to stabilize the microstructure with no collapse after numerous repeated lithiation-delithiation processes.

Keywords: Solution combustion method, ZnFe₂O₄, Glycine-to-nitrate ratio, Electrochemical performance, Lithium ion batteries.

1. INTRODUCTION

In recent decades, lithium ion batteries (LIBs) have been widely used in portable electronic devices and also essential to advanced electrical/hybrid vehicles over traditional rechargeable battery systems by virtue of their high energy density, long cycling lifetime, light weight and excellent safety[1-4]. Graphite is the most popular anode material for commercial LIBs. However, the low theoretical capacity of 372 mAh g^{-1} has reached its theoretical limit which cannot fulfill the increasing demands for LIBs with high power and high energy density. Therefore, further research is vital to develop novel materials combining suitable theoretical capacity and electrochemical stability.

Recently, various spinel Fe-based binary and ternary metal oxides nanomaterial have been investigated as anode materials due to their high specific capacity, low cost and environmental benign[5-8]. It is well known that the electrochemical performance of ferrites (MFe_2O_4 , M= transition metal) can be effectively impacted by their morphologies and microstructure, which are strongly depend on the experimental conditions and synthesis method[9]. For example, 1D MFe_2O_4 (M= Zn, Co, Ni) nanorods were obtained using a template-engaged reaction with $\beta\text{-FeOOH}$ nanorods for anode materials of lithium ion batteries. The reversible capacity of 800, 625 and 520 mAh g^{-1} were obtained for CoFe_2O_4 , ZnFe_2O_4 and NiFe_2O_4 , respectively, at the high current density of 1000 mAh g^{-1} after 300 cycles[10]. MgFe_2O_4 nanoparticals synthesized through a sol-gel method showed a reversible capacity of 474 mAh g^{-1} over 50 cycles[11]. ZnFe_2O_4 octahedrons fabricated by one-step hydrothermal method delivered a reversible capacity of 730 mAh g^{-1} after 300 cycles with the current density of 1000 mAh g^{-1} [12]. However, these methods indispensably demand long reaction time, multiple processing steps or special instrumentation. In addition, in order to control some special structures, a whole host of organic salts, surfactant or templates are added, which result in the high costs and environmental pollution [13].

Solution combustion synthesis (SCS) has attracted considerable attentions due to its cost-effective, facile synthesis of porous oxide particles with nanostructure and high homogeneity in a quick and simple way[13], where glycine is one kind of fuel and complexant to prevent inhomogeneous precipitation of individual components prior to combustion. As there were few reports on the effect of glycine content on product properties synthesis via SCS method[14-16], especially on the which is applied as anode materials in LIBs, it is worthwhile to probe the influencing factor of glycine-to-nitrate ration .

In this paper, ZnFe_2O_4 nanoparticles have been synthesized by SCS with different glycine-to-nitrate ratio ((G/N equals 0.5, 1.0 and 1.5, the samples named as A, B and C hereafter). The experiment results suggest that the G/N ratio is able to influence the crystalline, grain size and electrochemical properties for ZnFe_2O_4 . Compared with samples G/N= 0.5 and G/N= 1.5, the G/N =1.0 one exhibits higher crystallinity, excellent cycling stability and prominent rate capability in LIBs.

2. EXPERIMENTAL

2.1 Sample preparation

All chemicals were analytical grade and purchased from Sinopharm Chemcal Reagent Co., Ltd. and were used without further purification. In a typical synthesis process, 5 mmol $\text{Zn}(\text{NO}_3)_2 \cdot 6\text{H}_2\text{O}$ and

10 mmol $\text{Fe}(\text{NO}_3)_3 \cdot 9\text{H}_2\text{O}$ were dissolved in 60 mL deionized water. Then, according to G/N ratio 0.5, 1.0 and 1.5, about 7.5, 15 and 22.5 mmol glycine were added into the solution, respectively. The mixture was continuously stirred for 5 minutes until glycine dissolved entirely. The resultant solution was heated at 100 °C with constant stirring for 5 hours to transform the solution into a xerogel. The xerogel underwent self-propagating combustion progress formed a fluffy powder at 200 °C in 5 minutes. Finally, fluffy precursors were calcined in air at 700 °C for 2 hours in the muffle furnace at a heating rate of 4 °C min⁻¹ and the porous structure ZnFe_2O_4 nanoparticles were obtained after being cooled to room temperature.

2.2 Characterization

The crystal structure of as-prepared compounds were identified by X-ray diffraction (XRD) using a Rigaku MiniFlex II X-ray diffractometer with Cu $K\alpha$ radiation ($\lambda = 0.154178$ nm). Scanning electron microscope (SEM) micrographs were recorded on a FEI Nova NanoSEM 450 field emission scanning electron microscope at 15 kV. The xerogels was examined with TG-DSC on a NETZSCH STA 449F3 at 35–800 °C under air atmosphere. The heating rate was 5 °C min⁻¹. The residual quantity of element C and N in ZnFe_2O_4 were measured by Thermo Flash 2000. Transition electron microscope (TEM) images were taken using a Tecnai G2 TF30 S-Twin transmission electron microscopy at an accelerating voltage of 300 kV. The specific surface area of porous ZnFe_2O_4 was measured by the Brunauer–Emmett–Teller (BET) method using nitrogen adsorption on a Tristar 3000 system.

2.3 Electrochemical measurements

The electrochemical performances were performed using a standard CR2016 coin cell with lithium metal as counter electrode, a Celgard 2400 microporous polypropylene membrane as the separator, and a solution of 1 mol L⁻¹ LiPF₆ in ethylene carbonate/dimethyl carbonate (EC/DMC) with a volume ratio of 1:1 as electrolyte. Working electrodes were prepared with the composition of 70 wt.% ZnFe_2O_4 , 20 wt.% conductive carbon blacks (super P) as a conductive additive, and 10 wt.% polyvinylidene fluoride (PVDF). Galvanostatic charge-discharge cycling was performed in the range from 0.01 to 3.0 V versus Li/Li⁺ at current densities of 200 mA g⁻¹ with a Land BTI-40 (Wuhan, China) cell test system at room temperature. The rate capabilities of samples were tested at current from 100 to 1600 mA g⁻¹. Cyclic voltammetry (CV) measurements were conducted at a scan rate of 0.2 mV s⁻¹ in the voltage of 0.005–3.0 V (vs. Li/Li⁺) using Metrohm Autolab PGSTAT302N (Netherlands). Electrochemical impedance spectroscopy (EIS) curves were also collected on Metrohm Autolab PGSTAT302N with a frequency range from 0.01 Hz to 100 kHz.

3. RESULTS AND DISCUSSION

3.1. Structural and morphological characterization

Fig. 1 (a) manifests XRD patterns for the precursors of ZnFe_2O_4 . The diffraction peaks of precursor A are lower and wider than that of precursor B and C, which implies precursor A possesses

the poor crystallinity. That may attribute to the fuel-lean condition leading to relative low combustion temperature and milder reaction process than the other two samples. The situation was distinctly improved after calcination process. For precursor C, there are two extra peaks at 31.9° and 37.1° , which belong to the (220) and (311) plane of Fe_3O_4 . Compared with other two precursors, precursor B possesses the highest crystallinity without any impurity.

The XRD patterns of the as-prepared samples are shown in Fig. 1 (b). The impurity-free single phase and the diffraction peaks agreeing well with cubic spinel ZnFe_2O_4 (PDF Card, No. 22-1012) are observed in XRD patterns of sample A and B. And the sample B reveals sharper peaks than that of sample A. That means crystallinity of sample B is better than that of A under the similar synthetic process. As the G/N ratio raising to 1.5, characteristic peaks of Fe_2O_3 located at $2\theta = 27.3^\circ$, 33.3° , 35.8° , 41.0° , 49.6° and 54.2° corresponding to (012), (104), (110), (113), (024) and (116) begin to appear. Impurity phase Fe_2O_3 should be generated from Fe_3O_4 impurity phase in the precursor after calcination at 700°C .

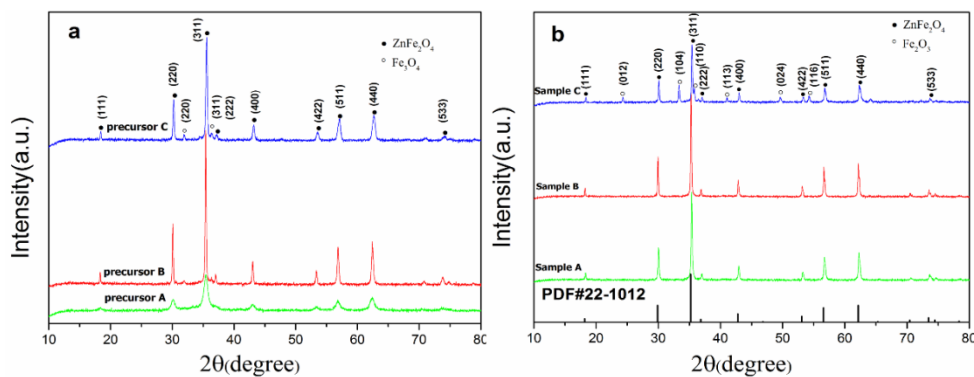


Figure 1. XRD patterns of precursors (a) and the as-prepared samples (b).

The combustion process of samples were examined by TG-DSC analysis. Only one mass loss step and endothermic peak at 174 , 157.9 and 166.4°C is observed for sample A, B and C each in Fig. 2, which implies that xerogel reacted at autoignition temperature and no other reaction occurred. The mass residual rate of sample B is 32.3% and sample A is 37.5% due to the minimum G/N ratio. In contrast, the residual loss rate of sample C is 31.5%. The heat flow corresponding to the DSC peaks of three samples are -10.98 , -22.15 and -21.47 mW mg^{-1} , respectively.

It is worth noting that $\text{Fe}(\text{NO}_3)_3 \cdot 9\text{H}_2\text{O}$ transforms into Fe_2O_3 at 166°C and it is close to the autoignition temperature of sample C[17]. That leads to the presence of Fe_2O_3 impurity in sample C. As the previous reports[16, 18], the heat is insufficiently generated and a high amount of carbonaceous material is left over during autoignition process in fuel rich condition. In addition, sample A with the highest N residual quantity indicates reaction between glycine and nitrate is insufficient. Meanwhile, the sample B releases the most heat which is indicative of a complete combustion.

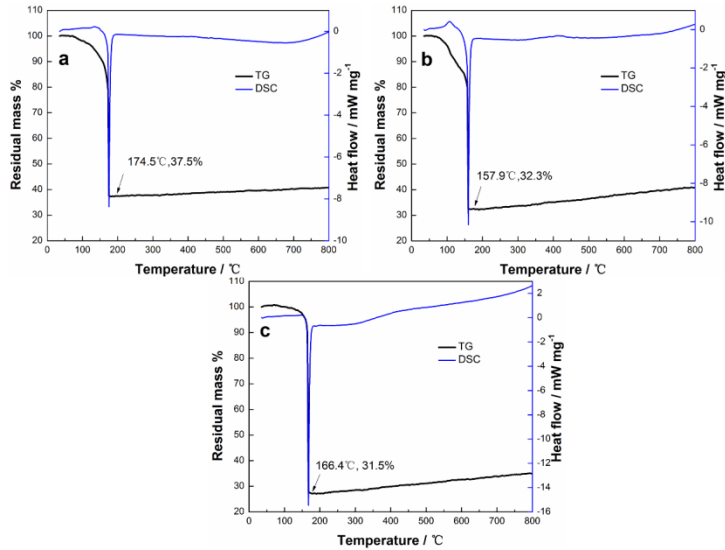


Figure 2. TG-DSC of sample A (a), B (b) and C (c).

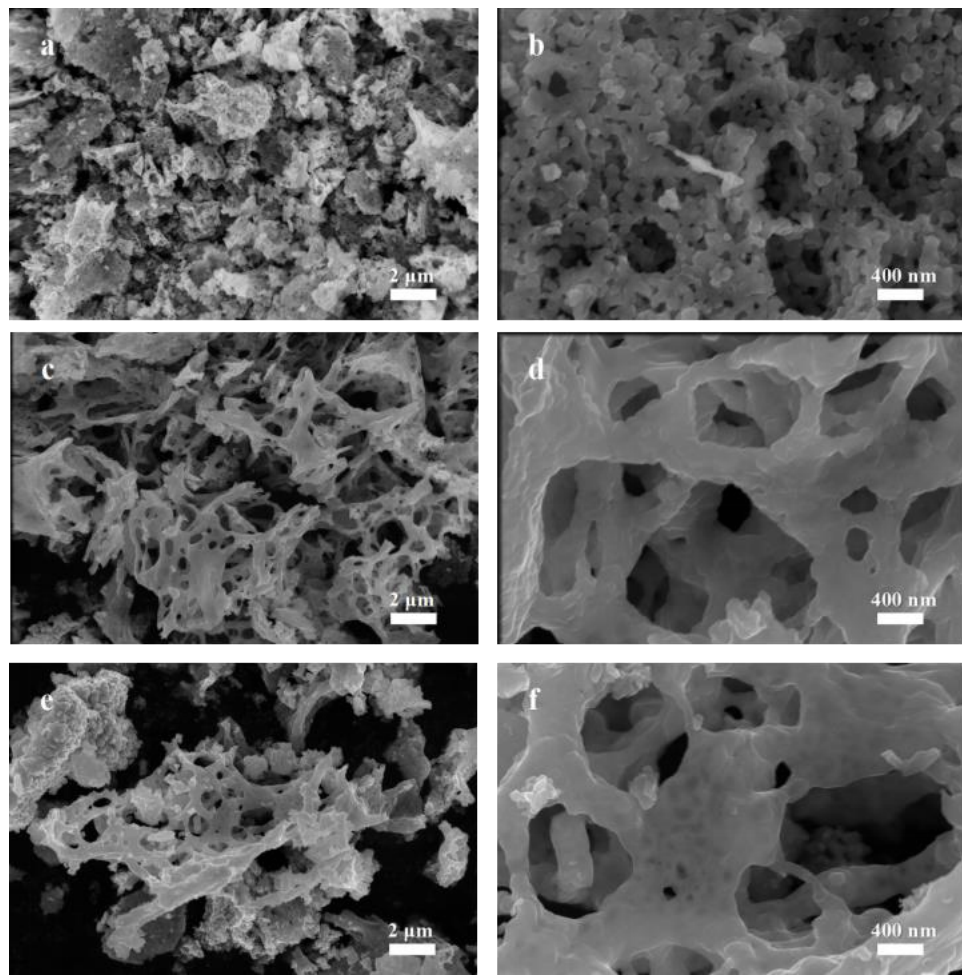


Figure 3. FESEM images of sample A (a and b), sample B (c and d) and sample C (e and f).

The morphologies and particle sizes of the as-prepared samples were characterized by FESEM. As shown in Fig. 3, the as-prepared materials present porous structure which is capable of buffering the volume expansion and making better contact between the electrode and electrolyte. Fig. 3 (a) and (b) reveal that sample A possesses the smaller size pores than the other two samples, which is probably ascribed to the less gas released during combustion as a result of fuel-deficient ratio. Sample B has plentiful pores with larger diameter than that of sample A. The number of pores of sample C is relatively few because of the particles aggregation. The average grain sizes of the compounds are in the range of 70~120 nm.

Table 1. Elemental ratio (atomic percent) of Zn and Fe in sample C.

	Fe (%)	Zn (%)
Point 1	70.38	29.61
Point 2	100	0

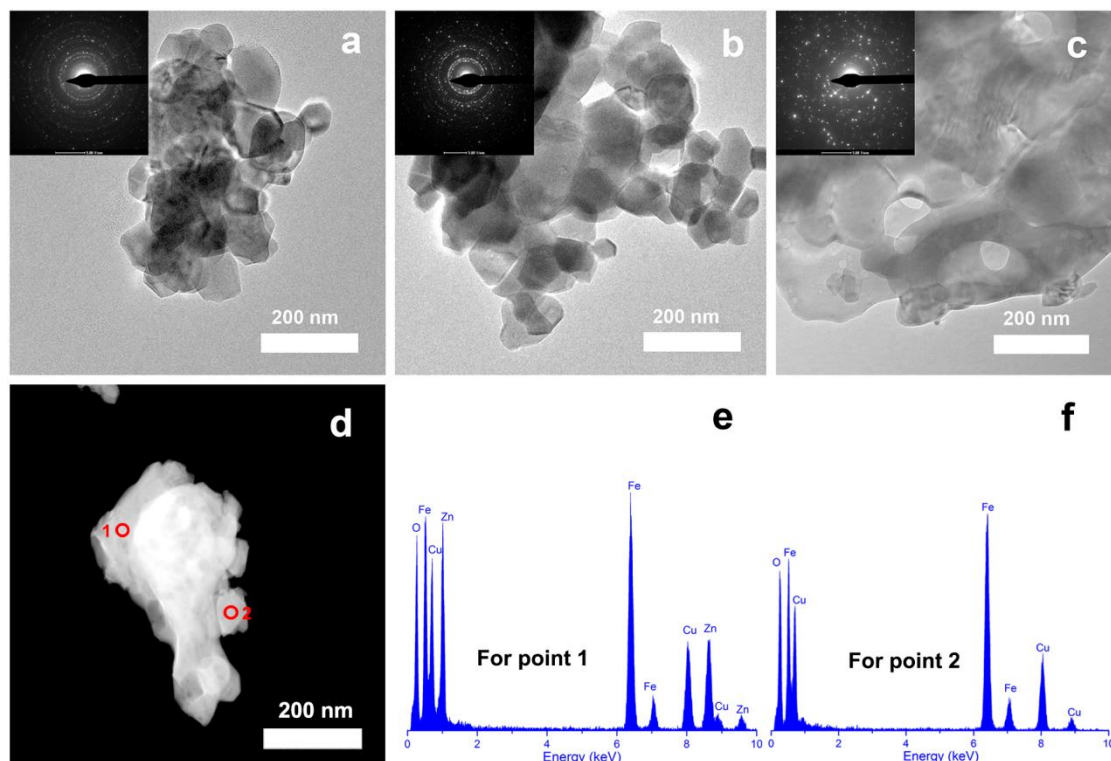


Figure 4. TEM micrographs of SCS synthesized sample A (a), sample B (b) and sample C (c), the inserts showing the SAED patterns, STEM (d) and corresponding EDX spectrums of sample C.

TEM images of the sample A, B and C shown in Fig. 4 was used to further investigate the size and agglomeration state of the ZnFe_2O_4 nanoparticles at various G/N ratio. As illustrated in Fig. 4 (a) and (b), the lattice of sample A and B stack together side by side and grain size is 100 nm around. However, grain boundary of the sample C is indistinct. Hence, the whole particle consists of

agglomerated nanocrystallites and the grain size is hardly measured. The selected area electron diffraction (SAED) patterns consisting of ring-type diffraction are inserted in Fig. 4. Sample B possesses the clearest diffuse rings, but for sample C there barely find one ring. That indicates crystallinity of three sample is in the order of B > A > C, which consistents with the result of XRD. To confirm the component of the sample C, EDX was carried out. Comparing Fig. 4 (e) and (f), it can be seen that the element Zn does not homogeneously distribute throughout sample C, which even not exist in point 2 as shown in Table 1. This further confirms that iron oxides impure phase can be formed in sample C.

Fig. 5 shows N_2 adsorption-desorption isotherm of sample A (a), B (b) and C (c). The isotherms can be indexed to type IV with hysteresis loops[19]. The specific surface areas calculated from N_2 isotherms at 77 K according to BET method were 4.3, 7.0 and $2.1\text{ m}^2\text{ g}^{-1}$, and the BJH adsorption cumulative volume of samples are $0.03, 0.032$ and $0.009\text{ cm}^3\text{ g}^{-1}$ for sample A, B and C, respectively. The fuel-deficient ratio of sample A results in less gas releasing and relatively low specific surface than sample B. Sample B possesses the largest specific surface which attributes to sufficient reaction between glycine and nitrate through appropriate ratio. The lowest specific surface of sample C is because of particles agglomeration with excess glycine. The results suggest that G/N ratio plays a crucial role in the formation of porous structure in combustion process. It is worth noting that the porous structure can ease the volume expansion during the charge-discharge processes and shorten the diffusion paths of lithium ions, what is more, it also can expand contact surface area between the electrode and electrolyte to benefit the lithiation-delithiation processes.

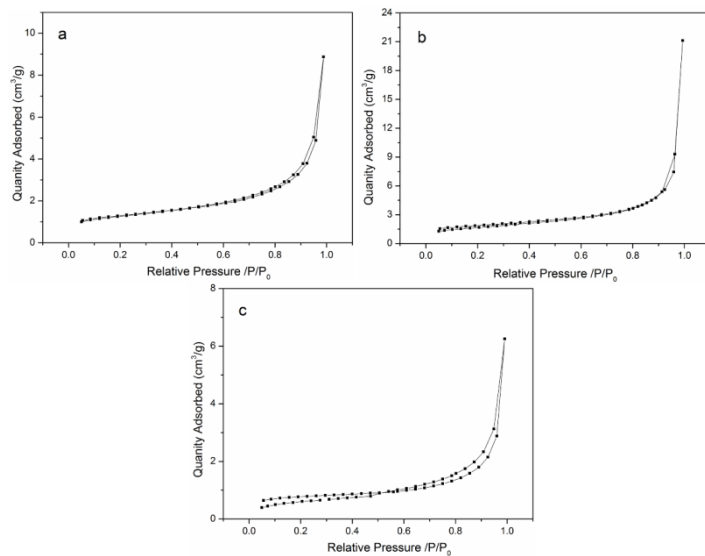


Figure 5. N_2 adsorption-desorption isotherm of sample A (a), B (b) and C (c).

3.2. Electrochemical performance

Cyclic voltammograms (CVs) of the $ZnFe_2O_4$ electrodes are given in Fig. 6. It can be found that a couple of oxidation-reduction peaks appear when the electrode potential scans from 0.005 to 3.0

V (vs. Li/Li⁺). For all samples, the first cycle is obviously different from subsequent cycles, indicating their different reaction mechanisms[20]. ZnFe₂O₄ transforms to Li_{0.5}ZnFe₂O₄ and then to Li₂ZnFe₂O₄ at the first discharge process, which is electrochemical reversibility (Eqs. (1) and (2)). For sample A and B, there is a sharp peak at around 0.62 V (Fig. (a) and (b)), whereas a peak is detected at around 0.71 V for CV curves of sample C (Fig. (c)).

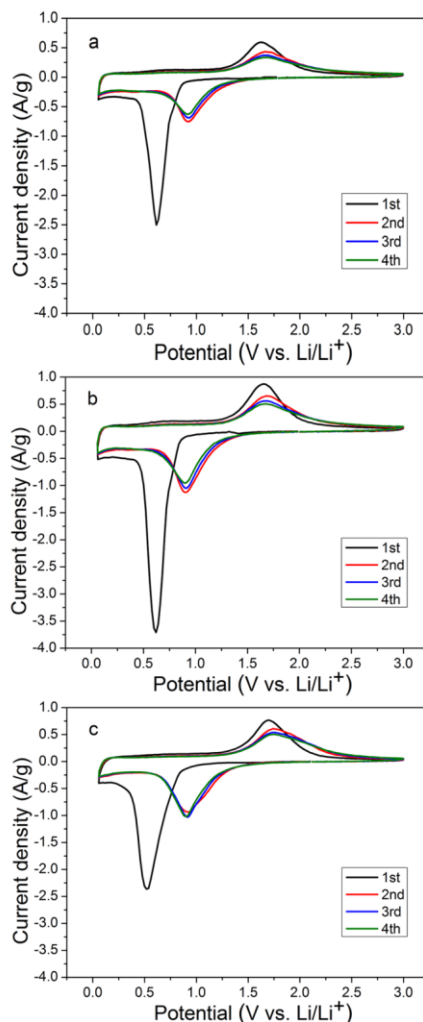


Figure 6. Cyclic voltammograms curves for sample A (a), sample B (b) and sample C (c) electrodes at a rate of 0.2 mV s⁻¹ in the voltage of 0.005~3.0 V vs. Li/Li⁺.

These peaks correspond to Li₂ZnFe₂O₄ consuming 6 Li⁺ ions formation of Zn⁰ and Fe⁰ and amorphous Li₂O, which is irreversible (Eq. (3)). Then Zn undergo a alloying process with Li to form Li-Zn alloy in discharged process (Eq. (4)). In the second cycle, the cathodic peaks shift to a higher voltage of \approx 0.90V, due to a structure rearrangement and associated with the reversible reduction of Fe³⁺ and Zn²⁺(Eqs. (5) and (6)). Simultaneously, sample A and B possess a broad peak at around 1.63 V in the first anodic process, while the anodic peak of sample C is at around 1.70 V, which correspond to the multistep oxidation of Zn⁰ and Fe⁰ to ZnO and Fe₂O₃, respectively. The relatively greater potential difference indicates the polarization of sample C is higher than the other two samples. The

anodic peak shift a bit to 1.70~1.76 V and are well overlapped in the subsequent cycles, indicating that good electrochemical reversibility and capacity retention for ZnFe₂O₄.

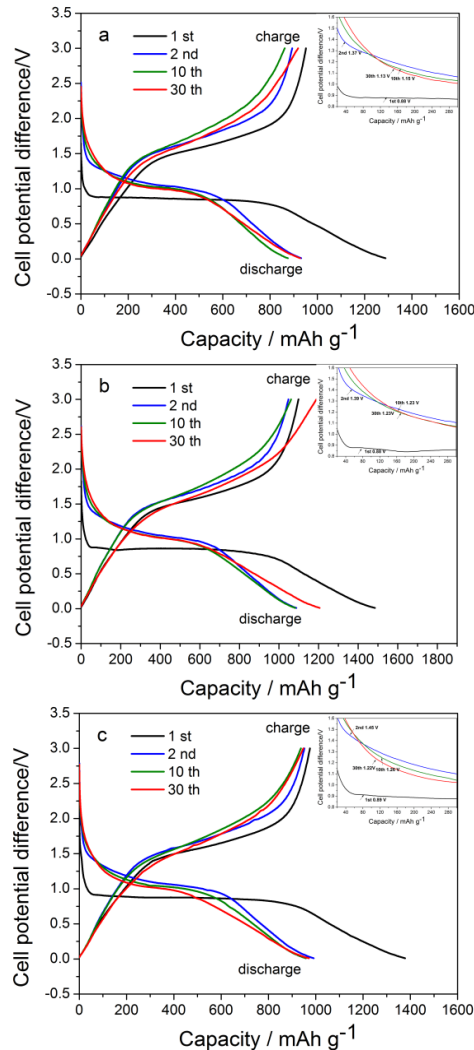


Figure 7. Charge-discharge plots of sample A (a), sample B (b) and sample C (c) for the 1st, 2nd, 10th, 30th at the specific current of 200 mA g⁻¹.

All these 9 lithium ions can be delivered in the recharge process however ZnFe₂O₄ cannot be restored[21, 22].

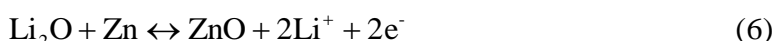
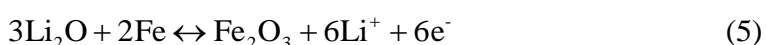
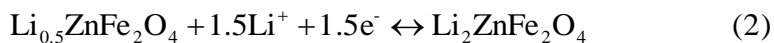


Fig. 7 depicts the charge-discharge profiles of all the compositions in the potential range of 0.01-3.0 V (vs. Li/Li⁺) at a current density of 200 mA g⁻¹, including the 1st cycle, 2nd cycle, 10th cycle

and 30th cycle. Sample B emerges its superiority from the first cycle to the last cycle. There is a voltage plateau at ca. 0.88 V in the first discharge process, the initial discharge and charge specific capacities of sample A, B and C are $1287.9/952 \text{ mAh g}^{-1}$, $1485.0/1098.6 \text{ mAh g}^{-1}$ and $1377.9/975.3 \text{ mAh g}^{-1}$, respectively. Due to the formation of a SEI layer on the electrode surface during the first discharge process, it can be observed that a large capacity loss between the first and subsequent cycles[21]. After the first cycle, a discharge gradual slope replaces the plateau. It can be found that the discharge gradual slope of 2nd , 10th and 30th for sample B are 1.37 V, 1.23 V and 1.25V, distinctly more stable than that of other two samples, which manifests that the polarization of sample B is lower than sample A and C and they need to be activated after several cycles. After 30 cycles, sample B is still able to deliver a specific capacity of $1189.3 \text{ mAh g}^{-1}$, which is higher than the second cycle. And the specific capacities of sample A and C maintain at 927.3 mAh g^{-1} and 970.9 mAh g^{-1} , close to the second cycle.

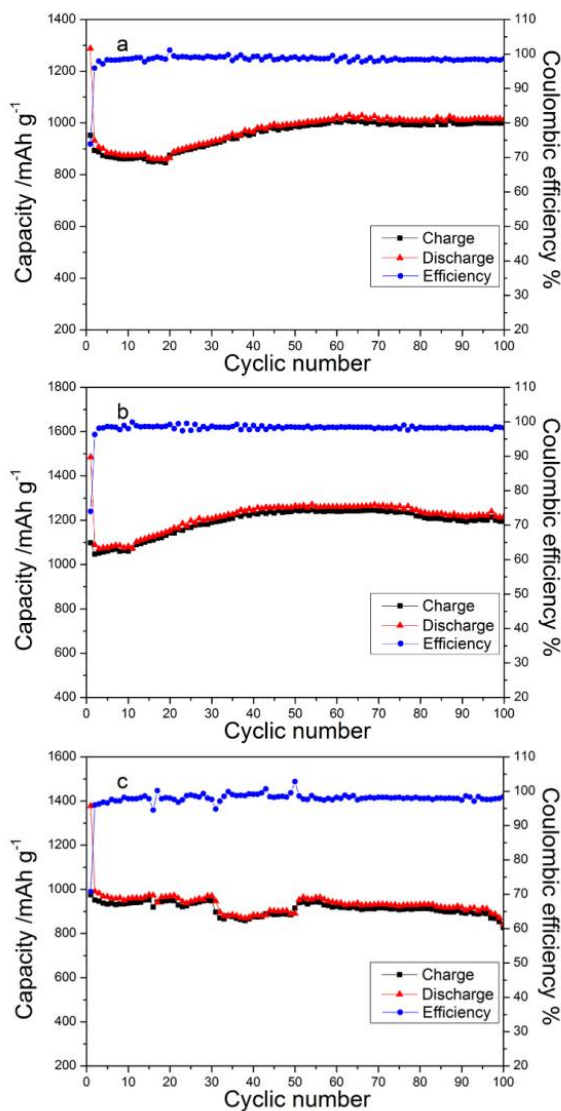


Figure 8. Comparison of cycling stability and coulombic efficiency of sample A (a), sample B (b) and sample C (c) at the specific current of 200 mA g^{-1} .

The cycling properties and coulombic efficiencies of samples with a current density of 200 mA g⁻¹ are displayed in Fig. 8. As can be seen from the Fig. 8, coulombic efficiencies of three samples keep a high level and the capacities barely declined at first 30 cycles. The cycling stability of sample A and B is outstanding in the whole 100 cycles, while the discharge capacity of sample C drops rapidly from 894.5 mA h g⁻¹ to 827.1 mA h g⁻¹ at the last 10 cycles manifesting its poor cycling stability. The capacities of sample A and B fading during the first few tens of cycles may be attributed to structural degradation and rearrangement with the formation of a polymeric gel-like film on the active materials[23]. The polymeric gel-like film is due to kinetically activated electrolyte decomposition, which can store excess Li⁺ ions through a so-called “pseudo-capacitance-type behavior”[24]. After 100 cycles, the curve (a) gradually drops and stays at 1013.7 mA h g⁻¹. As expected, sample B once again demonstrates its superior performance. The reversible specific capacity of sample B is ca. 1195.3 mA h g⁻¹, which is still higher than the capacity of the second cycle. Compared with sample A and C, sample B possesses more pores and higher crystalline without any impurity. Therefore, sample B reveals higher discharge capacity and excellent cycling stability.

Besides the high capacity and excellent cycling stability, the good rate capability is another important property for high-performance anode. The discharge capacities under different current densities in the 100 mA g⁻¹ to 1600 mA g⁻¹ range based three samples anodes are shown in Fig. 9. The sample B demonstrates considerably higher reversible capacities than sample A and C at all rates. It can be observed obviously decline of curves of sample A and C. However, curves of sample B decay slightly even a little rise at a same current density. The average discharge capacities at 1600 mA g⁻¹ of sample A, B and C were 789.6 mA h g⁻¹, 882.1 mA h g⁻¹ and 733.4 mA h g⁻¹, respectively. The restoration of three samples after high rate cycling is significant, when the current density returned to 100 mA g⁻¹, sample A, B and C recovered average discharge capacity of 1051.5 mA h g⁻¹, 1232.5 mA h g⁻¹, 1028.6 mA h g⁻¹. These results indicate that the sample B possesses better retention capability and rate performance than the other two, in conformity with previous tests.

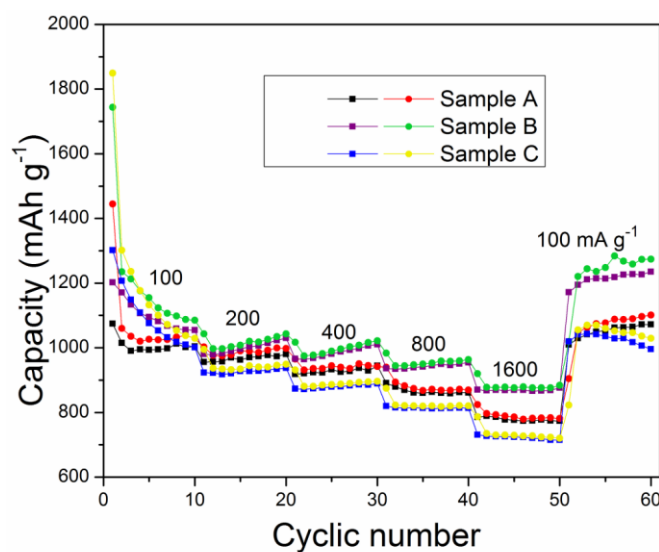


Figure 9. Rate performance of sample A, sample B and sample C at current densities from 100 to 1600 mA g⁻¹.

To further demonstrate the distinctions of three samples on the electrochemical performance, electrochemical impedance spectroscopy (EIS) measurements at different cycles were carried out. EIS may be considered as one of the most wildly and powerful analytical technique employed to study the kinetic parameters of the electrode process[34-36]. As shown in Fig. 10, the EIS diagram is composed of a depressed semicircle at high frequencies and a spike at low frequencies. The equivalent circuit for the observed Nyquist plots is shown in Fig. 10 (e)[37]. In this equivalent circuit, R_s indicates the ohmic resistance of electrolyte, R_b represents the electronic resistance of the active material and ionic conductivity in the electrode, R_{ct} corresponds to the charge transfer resistance; CPE represents the double-layer capacitance and W is the Warburg impedance. The values of R_b , R_{ct} and errors are listed in Table 3. The R_b values of three fresh cells are similar. However, R_b value of sample B cell is much smaller than others over 10 cycles. The R_{ct} values of sample B are lower than sample A and C regardless of the fresh or after 10 cycles at the current density of 200 mA g⁻¹. It indicates that the sample B may favor the electronic transmission and lead to a small internal resistance as well as good capacity retention. The above results prove that the electrochemical performance of sample B is better than the other two.

Table 2. Recently reported LIBs systems based on ferrite electrode.

Anode materials (R_s)	Synthetic method	Discharge capacity (mAh g ⁻¹) after several cycles	Current density (mA g ⁻¹)
Our work	Solution combustion synthesis method	1195.3, 100 cycles	200
Porous CoFe ₂ O ₄ nanosheets[25]	Thermal decomposition method	1147, 30 cycles	50
Cubic CoFe ₂ O ₄ nanoparticle[26]	Hydrothermal method	1133.5, 120 cycles	100
Nanostructured CuFe ₂ O ₄ [7]	Polymer-pyrolysis method	551.9, 100 cycles	100
CuFe ₂ O ₄ nanofibers[27]	Electrospinning method	536.3, 50 cycles	200
MnFe ₂ O ₄ -graphene nanocomposites[28]	Ultrasonic method	1017, 90 cycles	100
Mesoporous MnFe ₂ O ₄ microspheres[29]	Solvothermal method	712.2, 50 cycles	185.6
NiFe ₂ O ₄ nanofibers[30]	Electrospinning method	514, 60 cycles	50
NiFe ₂ O ₄ /C composite[31]	Polymer pyrolysis method	780, 40 cycles	116
MgFe ₂ O ₄ nanoparticles[32]	Sol-gel method	493, 50 cycles	90
Mesoporous MgFe ₂ O ₄ [33]	Combustion method	316.6, 30 cycles	300

Furthermore, the electrochemical performance of our porous ZnFe₂O₄ electrode was compared with that of other ferrite anode reported in the literature (Table 2). Compared with these reports, the advantages of the method in this paper are time and energy efficiency. More importantly, in this paper, the effects of different glycine-to-nitrate ratio on the combustion processes, phase composition, morphology and electrochemical performances of ZnFe₂O₄ are investigated in detail. When the glycine-to-nitrate ratio equals 1.0, the prepared sample obtains the highest crystallinity without any impurity and exhibits a higher rate capability and better reversibility as well. We believe the superior electrochemical performances can be attributed to the uniform porous structure in pure phase by using

the suitable quantity of glycine, which can not only ease the volume expansion during the charge-discharge processes but also provide more interstices for lithium ions insertion. Furthermore, the high crystallinity is able to stabilize the microstructure with no collapse after numerous repeated lithiation-delithiation processes.

Table 3. Resistance values and errors obtained from equivalent circuit fitting of experimental data for all samples.

	R _b (Ω)	R _{ct} (Ω)	Errors %
Sample A (fresh cell)	25.29	80.30	4.55
Sample A (after 10 cycles)	136.30	113.80	3.57
Sample B (fresh cell)	20.77	39.43	4.31
Sample B (after 10 cycles)	36.25	67.98	2.68
Sample C (fresh cell)	28.67	63.96	2.57
Sample C (after 10 cycles)	91.04	81.49	3.37

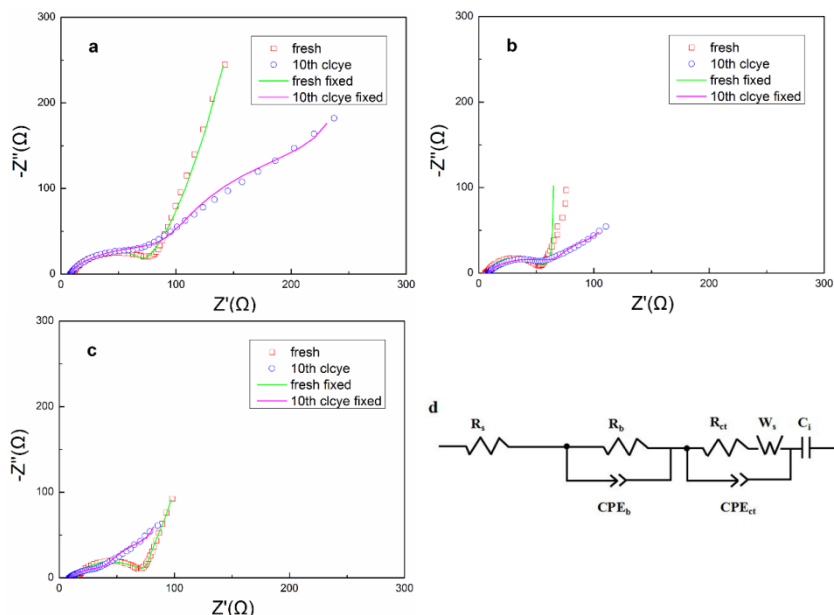


Figure 10. Nyquist plots of fresh and cycled electrode for sample A (a), sample B (b) and sample C (c) at open-circuit potential, (d) equivalent circuit model.

4. CONCLUSION

In summary, porous ZnFe₂O₄ porous nanoparticles have been fabricated by SCS with different glycine-to-nitrate ratio. The effects of glycine content on the combustion processes, phase composition, morphology and electrochemical properties of products have been discussed in detail in this paper. As the glycine-to-nitrate ratio rises, the number of pores also increases, and the crystallinity of products first rises then falls. Fe₂O₃ impurity is generated in sample C (glycine-to-nitrate ratio equals 1.5) which is due to the autoignition temperature close to the temperature of Fe(NO₃)₃·9H₂O transforming into Fe₂O₃ in combustion reaction. Compared with the other two

samples, sample B (glycine-to-nitrate ratio equals 1.0) possesses less residual quantity of element C and N and more heat release in combustion process, which implies complete combustion and bring with better crystallinity, larger specific surface area as a result. The electrochemical properties demonstrate that sample B electrode exhibits a high initial discharge capacity of $1485.0 \text{ mAh g}^{-1}$ and remains a stable reversible specific capacity of about $1195.3 \text{ mAh g}^{-1}$ after 100 cycles. Moreover, it also manifests superior high rate performance which recovers average discharge capacity to $1232.51 \text{ mAh g}^{-1}$ at the current density of 100 mA g^{-1} after 10 cycles at 1600 mA g^{-1} . As a result, we can get a conclusion that an appropriate glycine-to-nitrate ratio can obviously improve the performances of ZnFe_2O_4 , when the ratio is 1.0, the pure ZnFe_2O_4 with uniform porous structure and excellent electrochemical performance is easily obtained.

ACKNOWLEDGEMENT

The project was supported by National Natural Science Foundation of China (No.51604132) and the State Key Laboratory of Physical Chemistry of Solid Surfaces of Xiamen University (201506).

References

1. J. M. Tarascon, M. Armand, *Nature*, 414 (2001) 359.
2. F. Wu, N. Li, Y. Su, L. Zhang, L. Bao, J. Wang, L. Chen, Y. Zheng, L. Dai and J. Peng, *Nano Lett.*, 14 (2014) 3550.
3. C. Fu, G. Zhao, H. Zhang and S. Li, *Int. J. Electrochem. Sci.*, 8 (2013) 6269.
4. Q. Zhang and X. Li, *Int. J. Electrochem. Sci.*, 8 (2013) 6449.
5. Y. Sharma, N. Sharma, G.V.S. Rao and B.V.R. Chowdari, *Electrochim. Acta*, 53 (2008) 2380.
6. J. Mao, X. Hou, F. Huang, K. Shen, K.H. Lam, Q. Lu and S. Hu, *J. Alloys Compd.*, 676 (2016) 265.
7. L. Wu, Q. Xiao, Z. Li, G. Lei and P. Zhang and L. Wang, *Solid State Ionics*, 215 (2012) 24.
8. C. Fu, G. Zhao, H. Zhang and S. Li, *Int. J. Electrochem. Sci.*, 9 (2014) 46.
9. J. Ma, M. Zhan and K. Wang, *Acs Appl. Mater. Inter.*, 7 (2014) 563.
10. N. Wang, H. Xu, L. Chen, X. Gu, J. Yang and Y. Qian, *J. Power Sources*, 247 (2014) 163.
11. Y. Pan, Y. Zhang, X. Wei, C. Yuan, J. Yin, D. Cao and G. Wang, *Electrochim. Acta*, 109 (2013) 89.
12. Z. Xing, Z. Ju, J. Yang, H. Xu and Y. Qian, *Nano Res.*, 5 (2012) 477.
13. F. T. Li, J. Ran, M. Jaroniec and S. Z. Qiao, *Nanoscale*, 7 (2015) 17590.
14. S. R. Jain, K. C. Adiga and V.R.P. Verneker, *Combust. Flame*, 40 (1981) 71.
15. Q. Wang, H. Yue, T. Du, W. Zhang, Y. Qiao, H. Dong, Y. Yin and S. Yang, *Rsc Adv.*, 6 (2016) 35110.
16. C. H. Yan, Z. G. Xu, F. X. Cheng, Z. M. Wang, L. D. Sun, C. S. Liao and J. T. Jia, *Solid State Commun.*, 111 (1999) (5) 287.
17. M. Müller, J.C. Villalba and F.J. Anaissi, *Semina Ciências Exatas E Tecnológicas* 35 (2014) 9.
18. S. R. Nair, R. D. Purohit, A.K. Tyagi, P. K. Sinha, B. P. Sharma, *Mater. Res. Bull.* 43 (2008) 1573.
19. Sing S.W. K., *Pure Appl. Chem.*, 54 (1996) 2201.
20. L. Yao, X. Hou, S. Hu, Q. Ru, X. Tang, L. Zhao and D. Sun, *J. Solid State Electr.*, 17 (2013) 2055.
21. J. Xiao, G. Xu, S. G. Sun and S. Yang, *Part. Part. Syst. Char.*, 30 (2013) 893.
22. D. Yu, Y. Yang and H. Shao, *Electrochim. Acta*, 56 (2011) 9433.
23. Z. S. Wu, W. Ren, L. Wen, L. Gao, J. Zhao, Z. Chen, G. Zhou, F. Li and H. M. Cheng, *Acs Nano*, 4 (2010) 3187.
24. J. Wang, Q. Zhang, X. Li, B. Zhang, L. Mai and K. Zhang, *Nano Energy*, 12 (2015) 437.
25. X. Yao, J. Kong, X. Tang, D. Zhou, C. Zhao, R. Zhou, X. Lu, *Rsc Adv.* 4 (2014) 27488.
26. J. Mao, X. Hou, X. Wang, S. Hu, L. Xiang, *Mater. Lett.* (2015), p.652-655.

27. L. Luo, R. Cui, H. Qiao, K. Chen, Y. Fei, D. Li, Z. Pang, K. Liu, Q. Wei, *Electrochim. Acta* 144 (2014) 85.
28. Y. Xiao, J. Zai, L. Tao, B. Li, Q. Han, C. Yu, X. Qian, *Phys. Chem. Chem. Phys.* 15 (2013), 3939.
29. Z. Zhang, Y. Wang, Q. Tan, Z. Zhong, F. Su, *J. Colloid Interf. Sci.* 398 (2013) 185.
30. L. Luo, R. Cui, K. Liu, H. Qiao, Q. Wei, *Ionics* 21 (2015) 687.
31. Y. Ding, Y. Yang, H. Shao, *J. Power Sources* 244 (2013) 610.
32. N. Sivakumar, S.R.P. Gnanakan, K. Karthikeyan, S. Amaresh, W.S. Yoon, G.J. Park, Y.S. Lee, *J. Alloy Comp.* 509 (2011) 7038.
33. D. Narsimulu, B.N. Rao, M. Venkateswarlu, E.S. Srinadhu, N. Satyanarayana, *Ceram. Int.* 42 (2016) 16789.
34. M. V. Reddy, G. Prithvi, K. P. Loh and B.V.R. Chowdari, *Acs Appl. Mater. Inter.*, 6 (2014) 680.
35. M. V. Reddy, B.L.W. Wen, K. P. Loh and B.V.R. Chowdari, *Acs Appl. Mater. Inter.*, 5 (2013) 7777.
36. M.M. Rahman, J.Z. Wang, D. Wexler, Y.Y. Zhang, X.J. Li, S.L. Chou and H.K. Liu, *J. Solid State Electr.*, 14 (2010) 571.
37. S. H. Yeon, W. Ahn, S. Lim, K.H. Shin, C. S. Jin, J.D. Jeon, K. B. Kim and S. B. Park, *Carbon*, 78 (2014) 91.

© 2017 The Authors. Published by ESG (www.electrochemsci.org). This article is an open access article distributed under the terms and conditions of the Creative Commons Attribution license (<http://creativecommons.org/licenses/by/4.0/>).